

Metal Artifact Reduction for Polychromatic X-ray CT Based on a Beam-Hardening Corrector

Hyoung Suk Park, Dosik Hwang, and Jin Keun Seo*, *Member, IEEE*

Abstract—This paper proposes a new method to correct beam hardening artifacts caused by the presence of metal in polychromatic X-ray computed tomography (CT) without degrading the intact anatomical images. Metal artifacts due to beam-hardening, which are a consequence of X-ray beam polychromaticity, are becoming an increasingly important issue affecting CT scanning as medical implants become more common in a generally aging population. The associated higher-order beam-hardening factors can be corrected via analysis of the mismatch between measured sinogram data and the ideal forward projectors in CT reconstruction by considering the known geometry of high-attenuation objects. Without prior knowledge of the spectrum parameters or energy-dependent attenuation coefficients, the proposed correction allows the background CT image (i.e., the image before its corruption by metal artifacts) to be extracted from the uncorrected CT image. Computer simulations and phantom experiments demonstrate the effectiveness of the proposed method to alleviate beam hardening artifacts.

Index Terms—Beam hardening effect, computerized tomography, metal artifact reduction, radon transform.

I. INTRODUCTION

THIS work aims to improve computed tomography (CT) by reducing metal artifacts due to beam-hardening. They are generally generated by medical implants such as orthopedic implants, dental fillings, surgical clips, and coronary stents. Therefore, the increasing use of artificial prostheses and metallic implants combined with an aging population make the degradation of CT images by metal artifacts an increasingly common problem, and numerous research efforts have sought to reduce them. However, this issue is a major challenge facing CT imaging due to the difficulty in handling the nonlinearly varying projection data associated with the complex geometry of the metallic objects.

The presence of a metallic object in the scan field generates severe discrepancy between the projection data (P) and the

Radon transform ($\mathcal{R}f$). The projection data (for a two-dimensional parallel beam system) is given by the Lambert-Beer law [5], [21]:

$$P(\varphi, s) = -\ln \left(\int \eta(E) \exp \{-\mathcal{R}f_E(\varphi, s)\} dE \right) \quad (1)$$

where $f_E(\mathbf{x})$ denotes the attenuation coefficient at position $\mathbf{x} = (x_1, x_2)$ and at energy level E , $\eta(E)$ represents fractional energy at photon energy E in the spectrum of the X-ray source [16], [33]. The most widely used reconstruction method for CT is the filtered backprojection (FBP) algorithm [6]:

$$f_{\text{CT}}(\mathbf{x}) := \mathcal{R}^{-1}P(\mathbf{x}), \quad (2)$$

where \mathcal{R}^{-1} denotes the FBP operator.

Writing f_{target} as an unknown target image to be reconstructed, the uncorrected CT image f_{CT} can be decomposed into

$$f_{\text{CT}}(\mathbf{x}) := f_{\text{target}}(\mathbf{x}) + \mathcal{R}^{-1}[P - \mathcal{R}f_{\text{target}}](\mathbf{x}), \quad (3)$$

where $\mathcal{R}^{-1}[P - \mathcal{R}f_{\text{target}}]$ indicates the artifacts. In the presence of metallic objects, beam-hardening artifacts associated with the mismatch of $P - \mathcal{R}f_{\text{target}}$ cause severe bright and dark streaking artifacts in CT image, which greatly degrade the image quality. They depend mainly on the geometry of the metallic regions, the energy dependency of f_E for the metallic objects and the spectrum of the X-ray beam $\eta(E)$.

The artifact correction method proposed here uses shape information of the metallic implants to correct the mismatch $P - \mathcal{R}f_{\text{target}}$ in the FBP. Assuming that the metallic objects in the imaging slice occupy the region $D = \cup_{j=1}^N D_j$, we propose a beam hardening corrector $\phi_{D,\lambda}$ expressed by:

$$\phi_{D,\lambda} = -\mathcal{R}^{-1} \left[\ln \left(\frac{\sinh \left(\sum_{i=1}^N \lambda_i \mathcal{R}\chi_{D_i} \right)}{\sum_{i=1}^N \lambda_i \mathcal{R}\chi_{D_i}} \right) \right], \quad (4)$$

where λ_j is an unknown parameter that depends on the energy-dependent attenuation value of the object in D_j and the spectrum of the X-ray source. Here, χ_{D_j} denotes the characteristic function of D_j ; $\chi_D = 1$ in D_j and 0 otherwise. Numerical simulations show that this beam hardening corrector allows the background CT image (i.e., that which is not corrupted by metal artifacts due to beam-hardening) to be extracted from the uncorrected CT image f_{CT} . (See Fig. 1).

Let us now briefly discuss existing methods to suppress streaking artifacts due to metals. Examples of beam hardening correction methods include dual energy correction [2], [22],

Manuscript received July 07, 2015; revised September 09, 2015; accepted September 10, 2015. Date of publication September 15, 2015; date of current version February 01, 2016. This work was supported by Samsung Science and Technology Foundation (SSTF-BA1402-01). *Asterisk indicates corresponding author.*

H. S. Park is with the Department of Computational Science and Engineering, Yonsei University, Seoul 120-749, South Korea.

D. Hwang is with School of Electrical and Electronic Engineering, Yonsei University, Seoul 120-749, South Korea.

*J. K. Seo is with the Department of Computational Science and Engineering, Yonsei University, Seoul 120-749, South Korea (e-mail: seoj@yonsei.ac.kr).

Color versions of one or more of the figures in this paper are available online at <http://ieeexplore.ieee.org>.

Digital Object Identifier 10.1109/TMI.2015.2478905

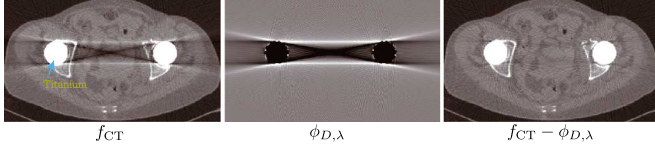


Fig. 1. Illustration of f_{CT} (left), $\phi_{D,\lambda}$ (middle) and corrected image $f_{CT} - \phi_{D,\lambda}$ (right) for the clinical CT image of pelvis containing two simulated metallic objects (titanium). The f_{CT} and $f_{CT} - \phi_{D,\lambda}$ are displayed with the same window center and width ($C = 2000 \text{ HU}/W = 8000 \text{ HU}$).

[40] and statistical iterative correction [11], [13], [25], [29], [38]. The former requires a lengthy post-processing and a higher dose of radiation compared with single-energy CT [9]. The latter requires prior information about the energy spectrum of the incident X-ray and energy-dependent attenuation coefficients of the materials. Kyriakou *et al.* [20] proposed empirical beam hardening correction (EBHC), which does not require such prior information. Various inpainting-based metal artifact reduction (MAR) methods have been suggested (e.g. interpolation [1], [4], [19], [23], [34], normalized interpolation (NMAR) [26], Poisson inpainting [30], wavelet [24], [41], [42], tissue-class model [3], and total variation (TV) [12], Euler's Elastica [15]). However, numerous previous studies using inpainting-based methods have found limited performance; inaccurate interpolation of the projection data can introduce additional streaking artifacts to the reconstructed image, and missing data caused by interpolation deteriorate morphological information in the region surrounding the metallic objects in the reconstructed image [26], [28].

The proposed artifact corrector is based on an analysis of the geometric characteristics of beam-hardening artifacts due to metals. It considers the geometry of the metal object (e.g., medical implants) and the corresponding artifacts. The performance of the proposed method is compared in numerical simulations and phantom experiments with those of other existing methods such as linear interpolation (LI) [19], NMAR and EBHC.

II. METHOD

The proposed beam hardening corrector (4) takes account of the geometry of high attenuation materials and the polychromatic X-ray beam, which is composed of the number of photons at different energies. Denoting by $I_0(E)$ the source intensity at energy level E , the detected X-ray intensity passing through the body along the line $L_{\varphi,s} := \{\mathbf{x} = (x_1, x_2) : x_1 \cos \varphi + x_2 \sin \varphi = s\}$ is detected by the Lambert-Beer's law:

$$I(E, \varphi, s) = I_0(E) \exp\{-\mathcal{R}f_E(\varphi, s)\}, \quad (5)$$

where $\mathcal{R}f_E(\varphi, s) = \int_{L_{\varphi,s}} f_E d\ell$ and $f_E(\mathbf{x})$ denotes the attenuation coefficient at position \mathbf{x} and at energy level E . Then the measured X-ray data for polychromatic X-ray source is expressed as

$$P(\varphi, s) = -\ln \frac{\int I(E, \varphi, s) dE}{\int I_0(E) dE} = -\ln \left(\int \eta(E) \exp\{-\mathcal{R}f_E(\varphi, s)\} dE \right), \quad (6)$$

where $\eta(E) = I_0(E) / \int I_0(E') dE'$ indicates the normalized energy spectrum of X-ray beam [35]. Now, we are ready to explain the main result of this paper.

A. Main Result: Beam Hardening Corrector

Regarding the target image as $f_{\text{target}} = f_{E_0}$ for an unknown energy level E_0 , the uncorrected CT image in (3) is expressed as

$$f_{CT}(\mathbf{x}) = f_{E_0}(\mathbf{x}) + \mathcal{R}^{-1}[P - \mathcal{R}f_{E_0}](\mathbf{x}) \quad (7)$$

Let $D = \cup_{j=1}^N D_j$ be a domain occupying the metal regions with its attenuation coefficient f_E^{metal} , and we first consider the case when the metallic subjects $D_j, j = 1, \dots, N$, have the same attenuation coefficient. Then the artifact term in (7) depends mainly on the geometry of D , the normalized energy spectrum of X-ray beam $\eta(E)$ and the energy dependency of f_E^{metal} . To be precise, the mismatch $P - \mathcal{R}f_{E_0}$ can be expressed as

$$\begin{aligned} [P - \mathcal{R}f_{E_0}](\varphi, s) &= -\ln \left(\int \eta(E) \exp\{-\mathcal{R}[f_E - f_{E_0}](\varphi, s)\} dE \right) \\ &= -\ln \left(\int \eta(E) \exp\left\{-\mathcal{R} \left[\int_{E_0}^E \frac{\partial f_{E'}}{\partial E'} dE' \right] (\varphi, s) \right\} dE \right) \end{aligned} \quad (8)$$

The attenuation coefficients of most soft tissues are more or less independent of X-ray energy, whereas the energy dependency of f_E^{metal} is high. For the ease of explanation, we assume that $f_E \approx f_{E_0}$ (energy independent) outside the metal region D ; that is, in the absence of metallic objects, beam hardening artifacts are assumed to be very small. Then, $(\partial f_E / \partial E)$ is supported approximately in D , and (8) can be approximated as

$$\begin{aligned} [P - \mathcal{R}f_{E_0}](\varphi, s) &\approx -\ln \left(\int \eta(E) \exp\left\{-\mathcal{R} \left[\int_{E_0}^E \frac{df_{E'}^{\text{metal}}}{dE'} dE' \chi_D \right] (\varphi, s) \right\} dE \right) \\ &\approx -\ln \left(\int \eta(E) \exp\{-\alpha(E - E_0) \mathcal{R} \chi_D(\varphi, s)\} dE \right), \end{aligned} \quad (9)$$

where $\alpha = (1/(E - E_0)) \int_{E_0}^E (df_{E'}^{\text{metal}}/dE') dE'$ depends on the spectral attenuation coefficient $f_{E'}^{\text{metal}}$ and E .

With a suitable choice of number $h \in \mathbb{R}$, it is crucial to observe the following approximation (See Fig. 2):

$$\int [\eta(E) - \tilde{\eta}_h(E)] \exp\{-\alpha(E - E_0) \mathcal{R} \chi_D(\varphi, s)\} dE \approx 0, \quad (10)$$

where $\tilde{\eta}_h$ is defined by

$$\tilde{\eta}_h(E) = \begin{cases} \frac{1}{2h} & \text{if } |E - E_0| < h \\ 0 & \text{otherwise} \end{cases} \quad (11)$$

In the above approximation (10), we use the two properties of the function $\eta - \tilde{\eta}_h$ as shown in shown in Fig. 2: (i) $\int \eta(E) -$

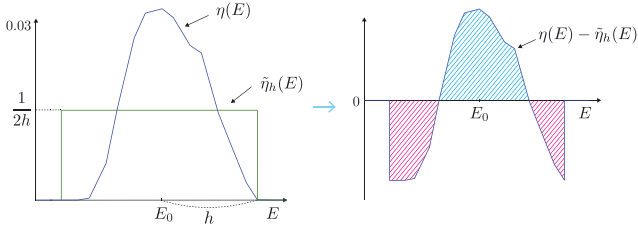


Fig. 2. Illustration of $\eta(E)$, $\tilde{\eta}_h(E)$ and $\eta(E) - \tilde{\eta}_h(E)$. $\eta(E)$ is the normalized X-ray spectrum for tungsten anode generated at a tube voltage of 80 kVp [8], and $\tilde{\eta}_h(E)$ in (11) is generated at $E_0 = 45$ keV and $h = 35$.

$\tilde{\eta}_h(E)dE = 0$; (ii) $\eta - \tilde{\eta}_h$ is approximately an even function with respect to $E - E_0$.

From (9) and (10), we have

$$\begin{aligned} [P - \mathcal{R}f_{E_0}](\varphi, s) &\approx -\ln \left(\int \tilde{\eta}_h(E) \exp \{ -\alpha(E - E_0) \mathcal{R}\chi_D(\varphi, s) \} dE \right) \\ &= -\ln \left(\frac{1}{2h} \int_{E_0-h}^{E_0+h} \exp \{ -\alpha(E - E_0) \mathcal{R}\chi_D(\varphi, s) \} dE \right) \\ &= -\ln \left(\frac{1}{2} \int_{-1}^1 \exp \{ \lambda t \mathcal{R}\chi_D(\varphi, s) \} dt \right), \end{aligned} \quad (12)$$

where $\lambda = -\alpha h$. The parameter λ is determined by the spectral attenuation coefficient f_E^{metal} and X-ray spectrum η . Assuming that λ is approximately independent of E (i.e. α is assumed to be independent of E), the last term in (12) can be approximated by

$$\begin{aligned} -\ln \left(\frac{1}{2} \int_{-1}^1 \exp \{ \lambda t \mathcal{R}\chi_D(\varphi, s) \} dt \right) &\approx -\ln \left(\frac{\sinh(\lambda \mathcal{R}\chi_D(\varphi, s))}{\lambda \mathcal{R}\chi_D(\varphi, s)} \right). \end{aligned} \quad (13)$$

From (12) and (13), the difference between f_{CT} and f_{E_0} can be expressed as

$$f_{CT}(\mathbf{x}) - f_{E_0}(\mathbf{x}) \approx \phi_{D,\lambda}(\mathbf{x}), \quad (14)$$

where $\phi_{D,\lambda}$ denotes the beam hardening corrector given by

$$\phi_{D,\lambda}(\mathbf{x}) = -\mathcal{R}^{-1} \left[\ln \left(\frac{\sinh(\lambda \mathcal{R}\chi_D)}{\lambda \mathcal{R}\chi_D} \right) \right] (\mathbf{x}) \quad (15)$$

Fig. 1 shows the numerical simulations of f_{CT} , $\phi_{D,\lambda}$ and the corrected image $f_{CT} - \phi_{D,\lambda}$ for the pelvis containing two simulated metallic objects (titanium). In this simulation, the projection data P in (1) is generated at energy range between 20–80 keV based on the experimental findings of attenuation coefficient in [17] and source spectra described in [8]. As shown in Fig. 1, the artifact corrector $\phi_{D,\lambda}$ compensates the streaking artifacts due to beam hardening from f_{CT} .

Fig. 3 shows the comparison between projection P in (1) and model data \tilde{P} based on equation (8)–(13), given by

$$\tilde{P}(\varphi, s) = \mathcal{R}f_{E_0}(\varphi, s) - \ln \left(\frac{\sinh(\alpha h \mathcal{R}\chi_D(\varphi, s))}{\alpha h \mathcal{R}\chi_D(\varphi, s)} \right) \quad (16)$$

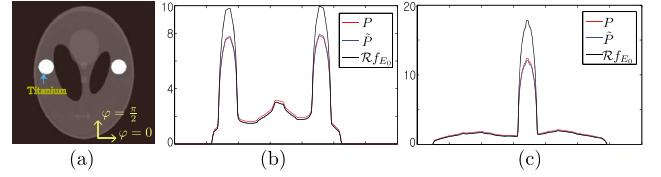


Fig. 3. Comparison between projection P in (1) and model data \tilde{P} in (16) at angle $\varphi = 0$ (b) and $\pi/2$ (c). In this simulation, projection data P is generated at energy range between 20–80 keV for Shepp-Logan phantom containing two titanium inserts (a).

Fig. 3 shows that \tilde{P} closely match with P . In this simulation, projection data P is generated at energy range between 20–80 keV for Shepp-Logan phantom containing two titanium inserts (Fig. 3(a)). The \tilde{P} is computed for $\alpha = (1/(80 - E_0)) \int_{E_0}^{80} (df_{E'}^{\text{metal}}/dE') dE'$, $E_0 = 50$ keV and $h = 25$.

B. Artifact Correction Algorithm

Based on the key characterization on the metal artifacts, we now explain the artifact correction algorithm. According to the analysis, streaking artifacts due to the presence of metals can be characterized in term of the geometry of the metallic subject D .

The proposed artifacts correction algorithm simply consists of the following two steps.

- 1) Segment the metal region D in f_{CT} .
- 2) Determine the best λ in such a way that $\phi_{D,\lambda}$ alleviates the streaking artifacts arising from beam hardening in f_{CT} optimally.

Let us focus on the step 2 since there are various segmentation techniques [3], [36], [39] to extract the metal region $D = \cup_{j=1}^N D_j$. For step 2, we propose the following misfit functional

$$\Phi(\lambda) = \int_{\mathbb{R}^2 \setminus \bar{D}} |W(\mathbf{x}) \nabla (f_{CT}(\mathbf{x}) - \phi_{D,\lambda}(\mathbf{x}))|^2 d\mathbf{x}, \quad (17)$$

where W is the weighting function chosen to impose more penalty on the streaking artifacts. We choose the weighting function W as

$$W(\mathbf{x}) = \nabla^2 \phi_{D,\lambda_0}(\mathbf{x}) \text{ for some fixed } \lambda_0$$

where ∇^2 is the Laplacian operator. This weighting function W is chosen based on the fact that the structure of streaking artifacts in $\phi_{D,\lambda}$ does not change with λ , which is the same of the streaking artifacts in f_{CT} due to the beam hardening associated with D . Recently, under the assumption that projection data P can be approximated as in (12), Park *et al.* [31], [32] have characterized that streaking artifacts due to beam hardening are straight lines tangent to the boundaries $\cup_{j=1}^N \partial D_j$ with touching at least two different points in the boundaries. In the presence of two disk shaped metallic objects in the field of view of CT (See the left image in Fig. 1), there are four tangent lines touching two different points on the boundary of D , along which streaking artifacts are produced in the reconstructed CT image f_{CT} . Here, $W(\mathbf{x}) = \nabla^2 \phi_{D,\lambda_0}(\mathbf{x})$ highlights the streaking structure more clearly, so that the weight function W gives more penalty on

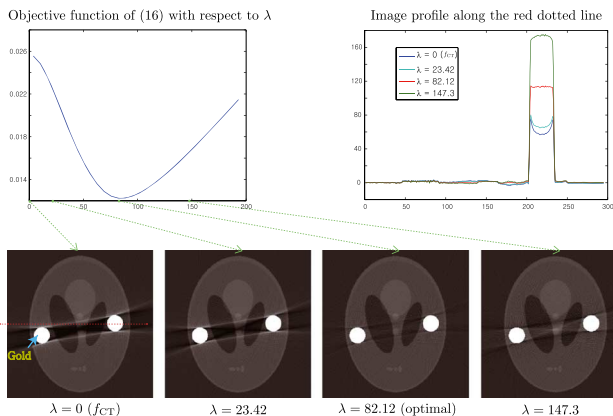


Fig. 4. Illustration of objective function of (18) with respect to λ (top left) for the Shepp-Logan phantom with two disk shaped metallic objects (gold), and corresponding corrected image $f_{CT} - \phi_{D,\lambda}$ (bottom three figures). The top right figure depicts the image profile of $f_{CT} - \phi_{D,\lambda}$ along the red dotted line. The streaking and cupping artifacts are significantly reduced at optimal $\lambda = 82.12$.

these tangent lines. The optimal parameter $\lambda > 0$ is determined by minimizing the functional $\Phi(\lambda)$:

$$\arg \min_{\lambda} \Phi(\lambda). \quad (18)$$

In our numerical simulations, the simple thresholding method suffices to extract the metal region D from f_{CT} . The nonlinear problem (18) is solved using the standard Newton's method with the initial value λ_0 . The initial value λ_0 can be determined by taking account of the energy range of incident X-ray and the attenuation coefficient of metallic material in the scan slice of CT. Fig. 4 illustrates the objective function of (18) with respect to $\lambda \in \mathbb{R}$ for the Shepp-Logan phantom with two disk shaped metallic objects (gold). As can be seen, the streaking and cupping artifacts are significantly reduced when $\lambda = 82.12$, which is the optimal value of the objective function of (18).

Now, we consider the general case of multiple metallic materials having the different variation of attenuation coefficients in the subregion D_i of the metal region D . Following the argument as before, we can derive the following artifact corrector $\phi_{D,\lambda}$ for multiple metallic objects:

$$\phi_{D,\lambda}(\mathbf{x}) = -\mathcal{R}^{-1} \left[\ln \left(\frac{\sinh \left(\sum_{i=1}^N \lambda_i \mathcal{R} \chi_{D_i} \right)}{\sum_{i=1}^N \lambda_i \mathcal{R} \chi_{D_i}} \right) \right] (\mathbf{x}), \quad (19)$$

where $\boldsymbol{\lambda} := (\lambda_1, \dots, \lambda_N)$ is a sequence of parameters depending on the metallic materials and incident X-ray source spectrum. The optimal parameter $\boldsymbol{\lambda} \in \mathbb{R}^N$ in (19) can be determined by solving the minimization problem (18).

Remark 2.1: In (19), there are N unknown parameters $\lambda_1, \dots, \lambda_N$. However, if $\cup_{j=1}^N \partial D_j$ consists of k different type of materials, then N unknown parameter $\boldsymbol{\lambda} = (\lambda_1, \dots, \lambda_N)$ in (19) can be simplified into k unknown parameters. For example, if D_1, \dots, D_m are gold and if D_{m+1}, \dots, D_N are iron, then (19) can be simplified into

$$\begin{aligned} & \phi_{D,(\lambda_1, \lambda_2)} \\ &= -\mathcal{R}^{-1} \left[\ln \left(\frac{\sinh \left(\lambda_1 \mathcal{R} \chi_{\cup_{i=1}^m D_i} + \lambda_2 \mathcal{R} \chi_{\cup_{i=m+1}^N D_i} \right)}{\lambda_1 \mathcal{R} \chi_{\cup_{i=1}^m D_i} + \lambda_2 \mathcal{R} \chi_{\cup_{i=m+1}^N D_i}} \right) \right] \end{aligned} \quad (20)$$

III. RESULTS

The proposed method is tested through numerical simulations and phantom experiments. The simulations consider the projection data P in (1) containing Poisson noise generated using the attenuation coefficients given in [17] and source spectra described in [8]. Other effects such as scattering and photon starvation are neglected, in order to focus on beam hardening due to metallic objects. The f_{CT} is computed by the standard FBP. The phantom studies use CT images acquired by an industrial cone-beam CT system (X-eye 7000 PCT, SEC CO., Korea). Note that the corrected CT images are obtained without using the projection data (or sinogram) of the CT scan.

A. Numerical simulations

Four different numerical phantoms containing metallic materials are used to test the proposed method. Fig. 5 illustrates its performance. First, second, third and fourth row show the reference, uncorrected, corrected CT images using the proposed method and difference images between corrected and reference images, respectively. Here, the reference images (artifact-free images) were generated by polychromatic simulation in (1) for segmented tissues and bones. Then, segmented metallic objects were added to the reference image. The proposed method successfully remove the streaking artifacts without losing morphological information, as shown in Fig. 5 (third row). Some artifacts are not completely removed owing to modeling errors in (14) such as the assumption of α being constant and neglect of the polychromatic attenuation of bone. However, beam hardening artifacts caused by bones (as shown in second column in Fig. 5) can be removed by applying the proposed method using segmented bone.

Fig. 6 shows the comparison among LI, NMAR, EBHC and the proposed method for jaw and pelvis phantom. Following the method in [26], prior image containing tissue and bone in NMAR method is obtained by simple thresholding after f_{CT} is smoothed with the Gaussian filter. In EBHC method, following the method in [20], we compute the parameter $c = (c_1, c_2, c_3) \in \mathbb{R}^3$ minimizing the following problem:

$$\begin{aligned} & \arg \min_c \int_{\mathbb{R}^2 \setminus \bar{D}} |\nabla(\mathcal{R}^{-1} P_w + c_1 f_{CT} \chi_D) \\ & + \nabla \left(\mathcal{R}^{-1} \left[c_2 P_w \mathcal{R} [f_{CT} \chi_D] + c_3 (\mathcal{R} [f_{CT} \chi_D])^2 \right] \right)| d\mathbf{x}, \end{aligned} \quad (21)$$

where P_w is the water-precorrected (or first order precorrected) projection data [18].

As shown in Fig. 6, the proposed method effectively reduces streaking artifacts in the reconstructed image caused by beam hardening, while the LI method creates new streaking artifacts due to the inherent nature of its interpolation technique [27]. The NMAR method also introduce streaking artifacts owing to the inappropriate normalization of projection data from regions near those containing data from metal [24]. Unlike both LI and NMAR, the proposed method preserves information from around metallic objects in the reconstructed image, because it

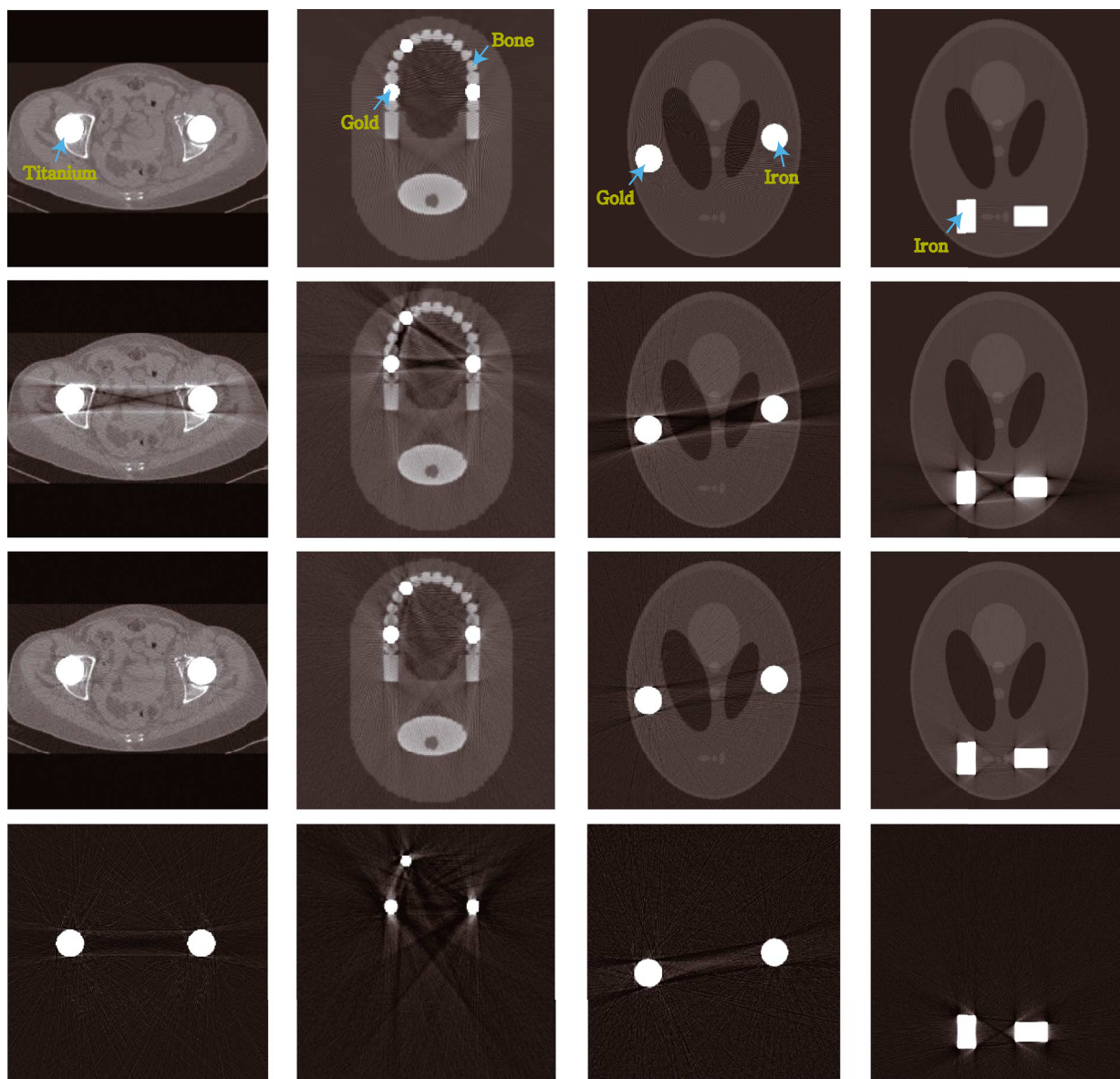


Fig. 5. Numerical simulation results using the proposed correction method. First, second and third row show the reference, uncorrected and corrected CT images using the proposed method, respectively. Fourth row shows the difference images between corrected and reference images. First column: clinical CT image of pelvis with the two disk-shaped numerical metallic objects (titanium). Second column: jaw phantom [37] with three disk-shaped metallic objects (gold). Third column: Shepp-Logan phantom with two different metallic objects (gold and iron). Fourth column: Shepp-Logan phantom with two rectangular metallic objects (iron). All uncorrected CT images (second row) are simulated at energy range between 20–80 keV ($C = 2000$ HU/W = 8000 HU for both CT images and difference images). The proposed method successfully reduces the streaking artifacts in the reconstructed images (See third row) without losing morphological information.

recovers only the region contaminated by beam hardening artifacts in the image space. The proposed method eliminates the streaking artifacts more clearly than the EBHC method, but at greater computational cost, because it requires backprojection at each iteration to compute the optimal parameter λ in (18), while EBHC requires one additional projection of the metallic objects and two additional backprojections.

B. Phantom Experiments

Fig. 7 shows experimental results using the proposed correction method for two experimental phantoms. Top phantom contains four different metallic rods (aluminum (Al), copper (Cu), molybdenum (Mo) and iron (Fe)), whereas bottom phantom consists of aluminum only. For the top phantom, we use the

following artifact corrector with the parameter $\lambda \in \mathbb{R}^4$ being chosen to minimize the misfit functional in (17):

$$\phi_{D,\lambda}(\mathbf{x}) = -\mathcal{R}^{-1} \left[\ln \left(\frac{\sinh \left(\sum_{i=1}^4 \lambda_i \mathcal{R} \chi_{D_i} \right)}{\sum_{i=1}^4 \lambda_i \mathcal{R} \chi_{D_i}} \right) \right] (\mathbf{x}), \quad (22)$$

where $\lambda_1 = 0.3$ for aluminum (D_1), $\lambda_2 = 4.1$ for copper (D_2), $\lambda_3 = 5.5$ for molybdenum (D_3) and $\lambda_4 = 3$ for iron (D_4). As shown in Fig. 7, the proposed method substantially enhances the CT image quality for both phantoms. The remaining streaking artifacts are mainly due to scattering, noise and our modeling error in (14).

Fig. 8 compares the proposed method with other existing correction methods such as NMAR and EBHC method for the experimental phantom. As shown in Fig. 8, the proposed method

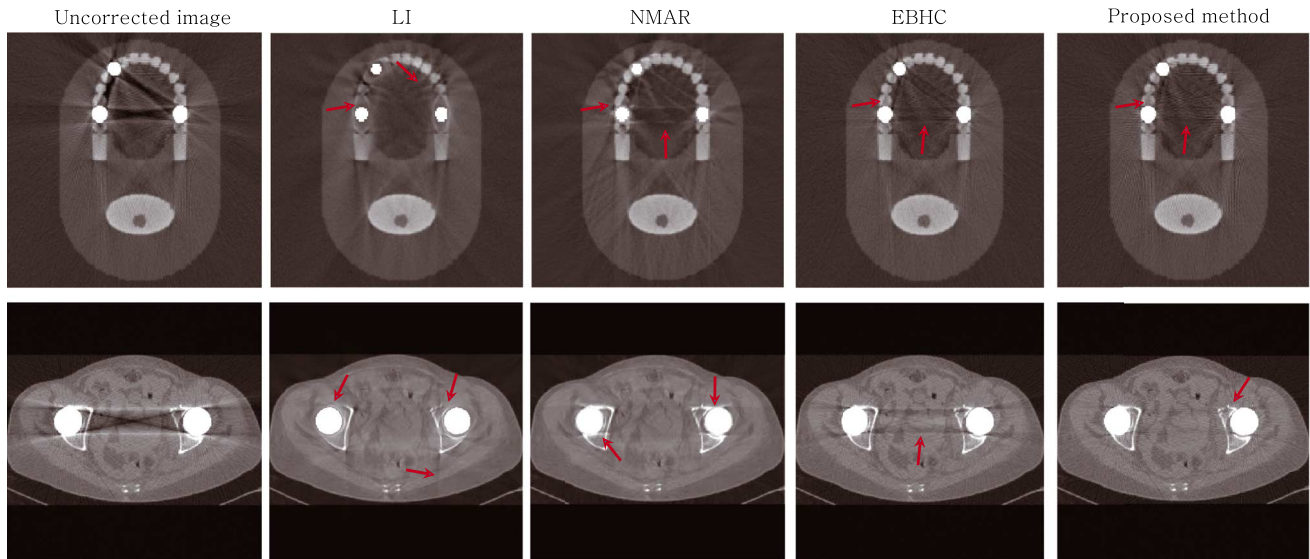


Fig. 6. Comparison among linear interpolation (LI), normalized metal artifacts reduction (NMAR), empirical beam hardening correction (EBHC) and the proposed method for jaw and pelvis phantom ($C = 2000 \text{ HU/W} = 8000 \text{ HU}$).

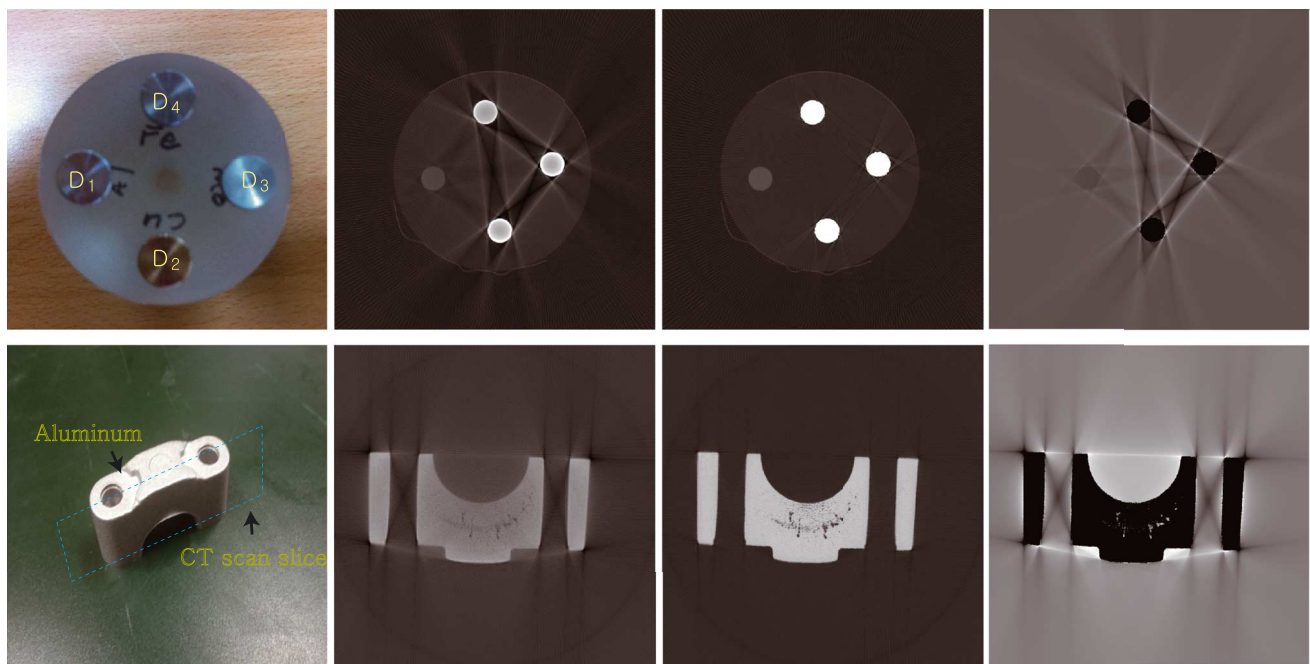


Fig. 7. Experimental results using the proposed correction method for two experimental phantoms. First, second, third and fourth column show picture of phantom, uncorrected images, corrected images and artifact correctors $\phi_{D,\lambda}$, respectively. Top phantom contains four different metallic rods (aluminum (Al), copper (Cu), molybdenum (Mo) and iron (Fe)), whereas bottom phantom consists of aluminum only. The uncorrected images are respectively acquired using 150 kVp at 650 μA ($C = 2000 \text{ HU/W} = 8000 \text{ HU}$ for CT images and $C = 0 \text{ HU/W} = 6000 \text{ HU}$ for difference image) for top phantom and 100 kVp at 400 μA ($C = 1000 \text{ HU/W} = 5000 \text{ HU}$ for CT images and $C = 0 \text{ HU/W} = 2000 \text{ HU}$ for difference image) for bottom phantom.

reduces the streaking artifacts more clearly than both NMAR and EBHC, while NMAR produces the new streaking artifacts resulting from inaccurate prior image.

Error estimation for numerical simulations and phantom experiment are performed. In the numerical simulations, the normalized root mean square difference (NRMSD) [24] between the corrected and reference image (first row in Fig. 5) is computed on the outside of the metal region D (See Table I). The experiment, generally lacking reference image, is analyzed by referencing the uncorrected image on the region (marked rROI in Fig. 8) far from the streaking artifacts. The mean absolute deviation (MAD) between the corrected and reference images is computed on the areas ROI1 and ROI2 marked in Fig. 8. In terms of both NRMSD and MAD, the proposed method shows better performance than the LI, NMAR and EBHC methods, as shown in Table I and Table II.

tion (MAD) between the corrected and reference images is computed on the areas ROI1 and ROI2 marked in Fig. 8. In terms of both NRMSD and MAD, the proposed method shows better performance than the LI, NMAR and EBHC methods, as shown in Table I and Table II.

IV. DISCUSSION AND CONCLUSION

This paper proposes a method of correcting metal artifacts due to beam hardening based on the observation that streaking artifacts arise mainly from the geometry of the boundaries of the metallic objects. The corrector ($\phi_{D,\lambda}$) is expressed with respect

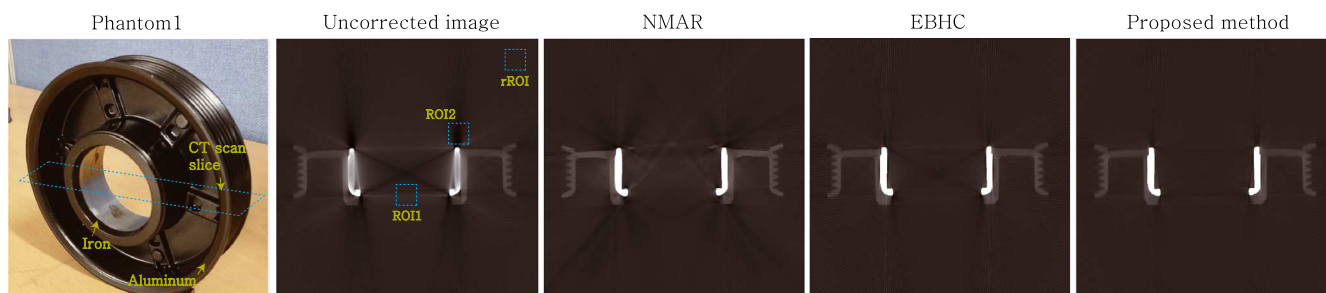


Fig. 8. Comparison among NMAR, EBHC and the proposed method for experimental phantom (marked Phantom1), which is made up of two materials-iron and aluminum based alloy. The uncorrected images is acquired using 100 kVp at 400 μ A ($C = 1000 \text{ HU/W} = 6000 \text{ HU}$).

TABLE I

QUANTITATIVE EVALUATION OF THE MAR METHODS FOR NUMERICAL PHANTOMS BASED ON THE NORMALIZED ROOT MEAN SQUARE DIFFERENCE (NRMSD) (%)

Phantom \ Method	Uncorrected (%)	LI	NMAR	EBHC	Proposed
Jaw	28.58	32.61	26.77	21.30	20.42
Pelvis	12.19	8.08	7.55	7.54	5.50

TABLE II

QUANTITATIVE EVALUATION OF THE MAR METHODS FOR EXPERIMENTAL PHANTOM BASED ON THE MEAN ABSOLUTE DEVIATION (MAD) (HU)

Phantom \ Method	Uncorrected (HU)	NMAR	EBHC	Proposed
Phantom1(ROI1)	135.76	114.72	101.56	95.18
Phantom1(ROI2)	378.98	156.95	130.76	115.27

to the geometry of the metallic objects (D) and an unknown parameter (λ) associated with their energy-dependent attenuation coefficient and the spectrum of the X-ray source. The parameter is computed by minimizing weighted least squares (18), with the weight being the Laplacian of the corrector to highlight the streaking artifacts generated by the metallic objects.

The proposed correction method successfully removes beam-hardening artifacts without the use of sinogram data. Neither does it require prior knowledge of energy spectra of the incident X-ray beam.

The performance of our method depends on segmenting the metallic objects. If the geometry of a metallic object is known, we only need to detect the position and orientation of the rigid object from the CT image (a rigid body in three-dimensional space has six degrees of freedom). Sparse template-based segmentation [7] can be used to extract the implant region. Hence, if the shapes of implants in the patient are known, the proposed method effectively remove the artifacts by incorporating prior knowledge of the implants and the corresponding artifacts. If the high-attenuation object has unknown geometry, its shape can be reconstructed by a threshold-based segmentation [10], [36].

Artifacts can arise in clinical CT from other causes such as scattering, photon noise, and nonlinear partial volume effects and further research is necessary to deal with them. Further experimental work with patients is also needed to establish the usefulness of the proposed method diagnosis and preoperative and presurgical assessment.

REFERENCES

- [1] M. Abdoli, M. R. Ay, A. Ahmadian, R. A. Dierckx, and H. Zaidi, "Reduction of dental filling metallic artifacts in CT-based attenuation correction of PET data using weighted virtual sinograms optimized by a genetic algorithm," *Med. Phys.*, vol. 37, pp. 6166–6177, 2010.
- [2] R. E. Alvarez and A. Macovski, "Energy-selective reconstructions in X-ray computerised tomography," *Phys. Med. Biol.*, vol. 21, p. 733, 1976.
- [3] M. Bal and L. Spies, "Metal artifact reduction in CT using tissue-class modeling and adaptive prefiltering," *Med. Phys.*, vol. 33, pp. 2852–2859, 2006.
- [4] M. Bazalova, L. Beaulieu, S. Palefsky, and F. Verhaegen, "Correction of CT artifacts and its influence on Monte Carlo dose calculations," *Med. Phys.*, vol. 34, pp. 2119–2132, 2007.
- [5] A. Beer, "Bestimmung der absorption des rothen lichts in farbigen flussigkeiten," *Annalen der Physik*, vol. 162, pp. 78–88, 1852.
- [6] R. N. Bracewell and A. C. Riddle, "Inversion of fan-beam scans in radio astronomy," *Astrophys. J.*, vol. 150, p. 427, 1967.
- [7] R. Brunelli, *Template Matching Techniques in Computer Vision: Theory and Practice*. New York: Wiley, 2009.
- [8] J. Bushberg, J. Seibert, E. Leidholdt Jr, and J. Boone, *The Essential Physics of Medical Imaging*. Philadelphia, PA: Lippincott Williams Wilkins, 2002.
- [9] E. Van, D. Castele, D. V. Dyck, J. Sijbers, and E. Raman, "A model-based correction method for beam-hardening artefacts in X-ray microtomography," *J. X-ray Sci. Technol.*, vol. 12, pp. 43–57, 2004.
- [10] J. Choi, K. S. Kim, M. W. Kim, W. Seong, and J. C. Ye, "Sparsity driven metal part reconstruction for artifact removal in dental CT," *J. X-Ray Sci. Technol.*, vol. 19, pp. 457–475, 2011.
- [11] B. De Man, J. Nuyts, P. Dupont, G. Marchal, and P. Suetens, "An iterative maximum-likelihood polychromatic algorithm for CT," *IEEE Trans. Med. Imag.*, vol. 20, no. 10, pp. 999–1008, Oct. 2001.
- [12] X. Duan *et al.*, "Metal artifact reduction in CT images by sinogram TV inpainting," in *IEEE Nucl. Sci. Symp. Conf. Rec.*, pp. 4175–4177.
- [13] I. A. Elbakri and J. A. Fessler, "Statistical image reconstruction for polyenergetic X-ray computed tomography," *IEEE Trans. Med. Imag.*, vol. 21, no. 2, pp. 89–99, Feb. 2002.
- [14] L. A. Feldkamp, L. C. Davis, and J. W. Kress, "Practical cone-beam algorithm," *J. Opt. Soc. Am. A, Opt. Image Sci.*, vol. 1, pp. 612–619, 1984.
- [15] J. Gu, L. Zhang, G. Yu, Y. Xing, and Z. Chen, "Metal artifacts reduction in CT images through Euler's elastica and curvature based sinogram inpainting," in *Proc. SPIE 6144, Med. Imag.*, 2006, pp. 614465–614465.
- [16] G. T. Herman and S. S. Trivedi, "A comparative study of two postreconstruction beam hardening correction methods," *IEEE Trans. Med. Imag.*, vol. 2, pp. 128–135, 1983.
- [17] J. H. Hubbell and S. M. Seltzer, "Tables of X-ray mass attenuation coefficients and mass energy-absorption coefficients," *Nat. Inst. Standards Technol.*, 1996.
- [18] M. Kachelrieß, K. Sourbelle, and W. A. Kalender, "Empirical cupping correction: A first order rawdata precorrection for cone-beam computed tomography," *Med. Phys.*, vol. 33, pp. 1269–1274, 2006.
- [19] W. A. Kalender, R. Hebel, and J. Ebersberger, "Reduction of CT artifacts caused by metallic implants," *Radiology*, vol. 164, pp. 576–577, 1987.
- [20] Y. Kyriakou, E. Meyer, D. Prell, and M. Kachelrieß, "Empirical beam hardening correction (EBHC) for CT," *Med. Phys.*, vol. 37, pp. 5179–5187, 2010.

- [21] J. H. Lambert and E. Anding, *Lamberts Photometrie: Photometria, Sive De Mensura et Gradibus Luminis, Colorum et Umbræ* no. V. 1-2, Ostwalds Klassiker der exakten Wissenschaften, 1892.
- [22] L. Lehmann *et al.*, "Generalized image combinations in dual kVp digital radiography," *Med. Phys.*, vol. 8, pp. 659–667, 1981.
- [23] R. M. Lewitt and R. H. T. Bates, "Image reconstruction from projections: IV: Projection completion methods (computational examples)," *Optik*, vol. 50, pp. 269–278, 1978.
- [24] A. Mehranian, M. R. Ay, A. Rahmim, and H. Zaidi, "X-ray CT metal artifact reduction using wavelet domain sparse regularization," *IEEE Trans. Medical Imaging*, vol. 32, pp. 1707–1722, 2013.
- [25] N. Menvielle, Y. Goussard, D. Orban, and G. Soulez, "Reduction of beam-hardening artifacts in X-ray CT," in *Proc. 27th Annu. Int. Conf. IEEE EMBS*, 2005, pp. 1865–1868.
- [26] E. Meyer, R. Raupach, M. Lell, B. Schmidt, and M. Kachelrieß, "Normalized metal artifact reduction (NMAR) in computed tomography," *Med. Phys.*, vol. 37, pp. 5482–5493, 2010.
- [27] E. Meyer, R. Raupach, B. Schmidt, A. H. Mahnken, and M. Kachelrieß, "Adaptive normalized metal artifact reduction (ANMAR) in computed tomography," in *Proc. IEEE Nucl. Sci. Symp. Med. Imag. Conf.*, 2011, pp. 2560–2565.
- [28] J. Müller and T. M. Buzug, "Spurious structures created by interpolation-based CT metal artifact reduction," in *Proc. SPIE Med. Imag.*, 2009, no. 7258, pp. 1Y1–1Y8.
- [29] J. A. O'Sullivan and J. Benac, "Alternating minimization algorithms for transmission tomography," *IEEE Trans. Med. Imag.*, vol. 26, pp. 283–297, 2007.
- [30] H. S. Park *et al.*, "Metal artifact reduction in CT by identifying missing data hidden in metals," *J. X-ray Sci. Technol.*, vol. 21, pp. 357–372, 2013.
- [31] H. S. Park, J. K. Choi, and J. K. Seo, "Characterization of metal artifacts in X-ray computed tomography," arXiv:1406.0318, 2014.
- [32] H. S. Park, Y. E. Chung, and J. K. Seo, "Computed tomographic beam hardening artefacts: Mathematical characterization and analysis," *Phil. Trans. R. Soc. A*, vol. 373, p. 20140388, 2015.
- [33] G. Poludniowski, G. Landry, F. DeBlois, P. Evans, and F. Verhaegen, "SpekCalc: A program to calculate photon spectra from tungsten anode X-ray tubes," *Phys. Med. Biol.*, vol. 54, pp. N433–N438, 2009.
- [34] J. C. Roeske, C. Lund, C. A. Pelizzari, X. Pan, and A. J. Mundt, "Reduction of computed tomography metal artifacts due to the Fletcher-Suit applicator in gynecology patients receiving intracavitary brachytherapy," *Brachytherapy*, vol. 2, pp. 207–214, 2003.
- [35] J. K. Seo and E. J. Woo, *Nonlinear Inverse Problems in Imaging*. New York: Wiley, 2012.
- [36] J. Wang and L. Xing, "A binary image reconstruction technique for accurate determination of the shape and location of metal objects in X-ray computed tomography," *J. X-ray Sci. Technol.*, vol. 18, pp. 403–414, 2010.
- [37] O. Watzke [Online]. Available: www.imp.uni-erlangen.de, Institute of Medical Physics. Erlangen, Germany, 2013.
- [38] J. F. Williamson *et al.*, "Prospects for quantitative computed tomography imaging in the presence of foreign metal bodies using statistical image reconstruction," *Med. Phys.*, vol. 29, pp. 2404–2418, 2002.
- [39] H. Yu *et al.*, "A segmentation-based method for metal artifact reduction," *Acad. Radiol.*, vol. 14, pp. 495–504, 2007.
- [40] L. Yu, S. Leng, and C. H. McCollough, "Dual-energy CT-based monochromatic imaging," *Am. J. Roentgenol.*, vol. 199, pp. S9–S15, 2012.
- [41] S. Zhao, K. T. Bae, B. Whiting, and G. Wang, "A wavelet method for metal artifact reduction with multiple metallic objects in the field of view," *J. X-ray Sci. Technol.*, vol. 10, pp. 67–76, 2001.
- [42] S. Zhao, D. D. Robeltson, G. Wang, B. Whiting, and K. T. Bae, "X-ray CT metal artifact reduction using wavelets: An application for imaging total hip prostheses," *IEEE Trans. Med. Imag.*, vol. 19, no. 12, pp. 1238–1247, Dec. 2000.